Research Square

Preprints are preliminary reports that have not undergone peer review.
They should not be considered conclusive, used to inform clinical practice,
or referenced by the media as validated information.

Giant piezoelectric response and electromechanical coupling in AlScN thin films via multi-scale lattice engineering

Zhenxiang Cheng

cheng@uow.edu.au

University of Wollongong https://orcid.org/0000-0003-4847-2907

Zhenyue Cheng

University of Jinan

Tong Liu

Shandong Provincial Key Laboratory of Preparation and Measurement of Building Materials, University of Jinan, MEMS Institute of Zibo National High-tech Development Zone

Daojian Su

University of Jinan

Changhong Yang

Shandong Provincial Key Laboratory of Preparation and Measurement of Building Materials, University of Jinan

Chuancheng Wu

University of Jinan

Yao Liu

Shandong University

Wei Sun

University of Jinan https://orcid.org/0009-0002-7023-5553

Shifeng Huang

Shandong Provincial Key Laboratory of Preparation and Measurement of Building Materials
https://orcid.org/0000-0002-9757-4267

Article

Keywords: AlScN thin films, lattice engineering, MEMS receivers, ultrasensitivity, low-frequency applications

Posted Date: March 19th, 2026

DOI: https://doi.org/10.21203/rs.3.rs-9122069/v1

License: This work is licensed under a Creative Commons Attribution 4.0 International License.
Read Full License

Additional Declarations: There is **NO** Competing Interest.

Version of Record: A version of this preprint was published at Nature Communications on August 10th, 2026. See the published version at https://doi.org/10.1038/s41467-026-76543-y.

Abstract

High-performance AlScN thin films are critical for next-generation lead-free piezoelectric applications. Here, exceptional electromechanical coupling and piezoelectric response are demonstrated in Al0.9Sc0.1N thin films via a multi-scale lattice engineering strategy. Post-growth rapid thermal annealing significantly boosts the piezoelectric coefficient to 15.0 pC N-1 and electromechanical coupling to 34.9%. This performance enhancement stems from a synergistic mechanism: a reduced c/a lattice ratio and homogenized nanodomain alignment, fundamentally underpinned by a transition toward higher bond ionicity as evidenced by reduced minimum electron density at the bond saddle points. Leveraging an industrial-grade 6-inch wafer process, these films exhibit tailored electromechanical characteristics with a resonance frequency of 368.2 kHz. The optimized piezoelectric response enables record-breaking acoustic sensitivity of -162.4 dB at 10 Hz and a noise floor of 59 dB at 1 kHz, with robust stability across diverse media and temperatures up to 150 °C. This work provides a scalable, mechanism-driven pathway for tailoring the electromechanical properties of AlScN thin films, addressing the long-standing challenge of high-fidelity weak signal detection in extreme environments.

1. Introduction

Piezoelectric micro-electromechanical systems (MEMS) exhibit remarkable advantages in passive operation, extreme miniaturization, and scalable manufacturability, effectively addressing the inherent constraints of conventional bulk materials, such as excessive dimensions, high power consumption, and integration complexities[1-3]. By leveraging efficient mechanical-to-electrical energy conversion, piezoelectric MEMS architectures have underpinned a new generation of precision acoustic transducers[4,5], intelligent robotic skins[6,7], environmental energy harvesters[8], and high-resolution medical imaging arrays systems[9]. As micro-sensor functionalities continue to evolve, piezoelectric MEMS are rapidly advancing to the forefront of autonomous sensing and ubiquitous computing.

In the realm of acoustic reception, piezoelectric MEMS have redefined the capabilities of transducers, particularly for low-frequency detection critical for long-range underwater surveillance and seismic monitoring[10,11]. These devices typically operate by converting low-frequency (≤1000 Hz) acoustic waves into electrical signals via thin-film piezoelectricity. While traditional materials like $Pb(Zr,Ti)O_3$ (PZT) and ZnO are widely utilized, they face significant limitations in low-frequency regimes. For instance, PZT-based cantilevers hydrophones often exhibit a dramatic sensitivity roll-off in the low frequencies, while ZnO sensors typically suffer from substantial signal attenuation due to their modest piezoelectric response and dielectric loss[12,13]. These challenges necessitate the exploration of novel material systems that can deliver high sensitivity and a flat response at low-frequencies without compromising structural integrity.

Recently, aluminum nitride (AlN) has emerged as a compelling lead-free alternative due to its high CMOS compatibility, inherent polarity (eliminating the need for high-voltage poling), exceptional thermal conductivity (200 $W\ m^{-1}\ K^{-1}$), and elevated operating temperature (up to 1150 °C)[14-18]. The

alloying of scandium (Sc) into the AlN lattice has been shown to exponentially enhance the piezoelectric response by softening the crystal lattice[1,19]. For example, $Al_{0.71}Sc_{0.29}N$ thin film can achieve a piezoelectric coefficient (d_{33}) of ~12.6 pC N^{-1}, more than double the value for pure AlN film[20,21]. Additionally, Sc substitution markedly increases the dielectric constant, with $\varepsilon_r \approx 15$ observed for $Al_{0.85}Sc_{0.15}N$ compared to $\varepsilon_r \approx 10$ for AlN[22,23]. However, a critical bottleneck exists: excessively high Sc concentration (typically >20%) often triggers phase instability, the formation of non-polar grains, and prohibitive fabrication cost[24-27]. Consequently, moderate Sc doping represents a more robust and feasible pathway for practical sensing applications, provided that the piezoelectric response can be further augmented through structural engineering. Nevertheless, the seamless integration of Sc-doped AlN into low-frequency MEMS is still impeded by the challenges in synthesizing high-performance thin films, achieving wafer-scale process compatibility, and optimizing device topologies.

In this work, we selected an AlN thin film containing approximately 10 at.% Sc (abbreviated as AlScN), which as demonstrated in our density functional theory (DFT) calculations (Supplementary Fig. S1 and Table S1) and supported by the previous literatures (Supplementary Table S2 and Fig. S2), exhibited an optimal ratio of piezoelectric coefficient (d_{33})/relative permittivity (ε_r) for high receiving sensitivity. Crucially, we demonstrate that post-growth rapid thermal annealing (RTA) dramatically boosts the piezoelectric performance, elevating the d_{33} from 8.2 pC N^{-1} in the as-grown (AG) state to 15.0 pC N^{-1}. This enhancement is shown to originate from a reduction in the lattice parameter ratio (c/a) and the promotion of highly ordered nanoscopic domain orientations. Leveraging a 6-inch wafer-scale fabrication process, we developed a MEMS chip integrating a 5 × 5 array of RTA-AlScN sensing elements. The packaged device achieves a record acoustic pressure sensitivity of -162.4 dB (re: 1 V μPa^{-1}) at 10 Hz and a noise equivalent pressure of 59 dB (re: 1 μPa $Hz^{-0.5}$) at 1kHz. Furthermore, the sensor demonstrates robust functionality across diverse media, including water, silicone oil, and solid ceramics, maintaining high fidelity at temperatures up to 150 °C. This study provides a scalable and high-performance framework for lead-free Sc-doped AlN based acoustic sensing in complex and extreme environments.

2. Results

2.1 Microstructure and electrical performance of AlScN thin films

To investigate the effects of Sc doping and the **RTA** process on the crystalline structure of AlScN, X-ray diffraction (XRD) was performed. As shown in Fig. 1a, all samples exhibit a sharp (002) diffraction peak according to the standard wurtzite AlN pattern (JCPDS 76-0565), indicating a high degree of *c*-axis orientation. This is attributed to the high kinetic energy of sputtered particles during the deposition process[28,29]. Scanning electron microscopy (SEM) reveals both AG and RTA treated AlScN films possess uniform, spherical grains (Fig. 1bi and Supplementary Fig. S3a). Notably, the average grain size of RTA-AlScN (100 nm) is significantly larger than previously reported values for AlScN thin film with similar Sc content ($Al_{0.90}Sc_{0.10}N$ ~ 50 nm, $Al_{0.85}Sc_{0.15}N$ ~ 30 nm)[25,30]. Cross-sectional SEM images further confirm that both AG-AlScN and RTA-AlScN films feature well-defined columnar grains with thicknesses of

approximately 1 μm (Fig. 1bii and Supplementary Fig. S3b). Guided by our simulation results, this thickness was optimized to achieve a low resonant frequency of 390 kHz and a relatively high surface charge output (5.74×10^{-17} C), while ensuring mechanical robustness for practical applications (Supplementary Fig. S4)[31]. The chemical composition and element distribution were further verified by EDS and XPS (Supplementary Fig. S5 and S6).

Atomic-scale structural insights were obtained via high-angle annular dark-field scanning transmission electron microscopy (HAADF-STEM), providing high-precision atomic position measurements with uncertainties below 50 pm. As shown in Fig. 1c, d, N and Al(Sc) atoms form alternating hexagonal close-packed layers along the *c*-axis. Each Al(Sc) atom resides in a tetrahedral arrangement with four neighboring N atoms; this coordination confirms an “N-polar” growth direction, with the permanent dipole moment oriented toward the substrate. Critically, this N-polar characteristic in the AG-AlScN film remains stable and unchanged after RTA treatment. Statistical analysis of the lattice parameters across multiple regions (Supplementary Fig. S7, S8) reveals that following RTA, both *a* and *c* lattice parameters exhibit an increasing trend (Fig. 1e, f). The average *a*-axis parameter rose significantly from 3.163 Å to 3.279 Å, while the *c*-axis parameter increased marginally from 4.931 Å to 4.951 Å. The expansion of the *a*-axis in RTA-AlScN is attributed to stress relaxation, as **post-growth RTA** weakens the transverse interaction forces between adjacent columnar grains[32]. Consequently, the *c*/*a* ratio of RTA-AlScN decreased to 1.510 compared with 1.559 for AG-AlScN (Supplementary Table S3). RTA at high temperatures promotes the substitution of larger Sc^{3+} ions into Al^{3+} sites and the relaxation of epitaxial strain, driving the lattice towards a flatter, more frustrated hexagonal state with a reduced *c/a* ratio (Supplementary Fig. S9).

The improved piezoelectricity is fundamentally rooted in the synergistic evolution of chemical bonding and lattice symmetry. As corroborated by our DFT calculations (Supplementary Fig. S1f), Sc substitution reduces the minimum electron density (MED) at the bond saddle point—from 0.195 in pure AlN to 0.178 in $Al_{0.875}Sc_{0.125}N$—indicating a transition toward higher bond ionicity (weakened covalency). This lattice softening, characterized by decreased MED and electron localization function (ELF) values, facilitates a more compliant structural response to external strain. While Sc substitution establishes the chemical foundation for this softening, the RTA process serves as a structural trigger that further destabilizes the cation position via *c/a* ratio reduction. This dual-effect—combining intrinsic bonding modification with extrinsic lattice strain engineering—collectively drives the material toward a metastable state with exceptionally high polarizability. Theoretically, the lower *c*/*a* ratio resulting from this modified bonding state enhances polarization-strain coupling coefficient (e_{33}) and the polarization-electric field coupling coefficient (χ_{33}), thereby significantly boosting the effective piezoelectric coefficient ($d_{33} \approx \varepsilon_0 e_{33} \chi_{33}$)[33-35].

To characterize the effective electromechanical coupling coefficient (k_t^2), capacitance-electric field (*C*-*E*) loops were measured (Fig. 2a). The extracted k_t^2 values for RTA-AlScN reached 34.9%, a substantial improvement over the 14.1% of AG-AlScN, outperforming reported values for AlScN with Sc concentrations exceeding 30% (Fig. 2b). The d_{33} reached 15.0 pC N^{-1} for RTA-AlScN, representing a 2.5-fold enhancement over pure AlN (6 pC N^{-1}, Supplementary Fig. S10) and outperforming most reported

Sc-doped AlN materials (Fig. 2b). This performance remains highly uniform across the 6-inch wafer, with a d_{33} variation of less than 0.7% (Supplementary Fig. S11), highlighting its suitability for mass production. Additionally, the RTA-AlScN film exhibits a relative permittivity (ε_r) of 16 and a remarkable low dielectric loss (tan δ) of < 0.0006 at 1 kHz (Supplementary Fig. S12).

Surface topography evaluated by AFM (Fig. 2c) shows that RTA maintains high surface quality (RMS roughness of 0.65 nm). Figure 2d compares the out-of-plane PFM amplitude and phase images. While the AG-AlScN film reveals disordered nanodomains—evidenced by a high density of randomly oriented spots, indicating non-uniform piezoelectric activity—the RTA-AlScN film exhibits a marked reduction in these features and a high overall amplitude. This correlates with the enhanced *c*-axis ordering of nanodomains, a process intrinsically supported by the lowered ferroelectric switching barrier resulting from the increased bond ionicity and lattice flattening. This facilitates easier dipole rotation and long-range ordering during the thermal process. The distinct phase contrast confirms effective domain-switching under bias, successfully transitioning the central region from the “N-polar” state to the “Al(Sc)-polar” state[36,37]. Furthermore, RTA-AlScN displays superior ferroelectric behavior with a high remanent polarization (P_r ~107 μC cm^{-2}) and robust fatigue endurance (~10^5 cycles) (Supplementary Fig. S13).

2.2 Finite element simulation design

To guide the structural design of the MEMS receiver, we performed multiphysics coupling finite element analysis (FEA) of a single sensing element. The cross-sectional schematic in Fig. 3a depicts the multilayer architecture of the sensing element, which is integrated on an SOI substrate and comprises an AlN seed layer, Cr/Mo electrodes, and an AlScN piezoelectric functional layer. In piezoelectric MEMS transducers, a back cavity must be engineered beneath the piezoelectric membrane to release mechanical constraints and enable structural deformation. We first optimized the cavity diameter, as shown in the simulation results in Fig. 3a. As the back cavity radius (R_C) increases, the resonant frequency of the diaphragm consistently decreases. However, an excessively large R_C can compromise mechanical reliability, potentially leading to fatigue and fracture under continuous acoustic excitation. Balancing the requirements for low-frequency sensitivity and structural durability, a R_C of 250 μm was selected to ensure a sufficiently low resonant frequency while maintaining structural integrity.

With R_C fixed at 250 μm, we further investigated the dependencies of the induced charge and resonant frequency on the back cavity-to-(piezoelectric film and top electrode) ratio ($R_C/R_{PF\&TE}$) and (back cavity and piezoelectric film)-to-top electrode ($R_{C\&PF}/R_{TE}$) ratio. As illustrated in Fig. 3b, the total charge on the electrode surface initially increases with both $R_C/R_{PF\&TE}$ and $R_{C\&PF}/R_{TE}$, peaking at a ratio 1.25, before exhibiting a slightly decline. Conversely, the resonant frequency follows an opposite trend. At an $R_C/R_{PF\&TE}$ ratio of 1.25, the device achieves an optimal combination of a low resonant frequency (349.0 kHz) and a maximum induced charge (3.4×10^{-16} C).

Notably, at $R_C/R_{PF\&TE}$ = 1.25, the surface charge distribution exhibits a uniformly positive character (Fig. 3c), which supports the maximization of the total harvested charge. This phenomenon is attributed to the optimized distribution of compressive stress across the AlScN film under this configuration (Fig. 3d). For comparison, the results for $R_C/R_{PF\&TE}$ ratios of 1.0 and 1.5 are provided in Supplementary Fig. S14, S15. Similarly, at $R_{C\&PF}/R_{TE}$ = 1.25, the film also exhibits positive surface charges (Fig. 3e) and compressive stress in the top electrode (Fig. 3f). Comparative cases for $R_{C\&PF}/R_{TE}$ at 1.0 and 1.5 are detailed in Supplementary Fig. S16, S17. Nevertheless, the $R_{C\&PF}/R_{TE}$ = 1.25 configuration remains superior, providing a lower resonant frequency and higher charge density.

Using this optimized configuration, we simulated the device response under an applied acoustic field of 1 Pa at 1 kHz (source positioned 1 m above the sensor). These simulations reveal the relationship between external acoustic pressure and the resulting charge density distribution. Under the simulated acoustic field (Fig. 3g), the receiver undergoes predictable mechanical stress and deformation (Fig. 3h). As acoustic pressure of approximately 116 dB (*pref* = 1 μPa) induces a surface charge density ranging from 0.5×10^{-5} to 2.5×10^{-5} C m^{-2} (Fig. 3i). This rigorous FEA framework validates the design's effectiveness for high-quality low-frequency acoustic sensing.

2.3 Structure design and fabrication of MEMS device

Based on the aforementioned FEA optimization and superior piezoelectric properties of the RTA-AlScN film, we proceeded with the micro-fabrication and characterization of the devices on a 6-inch wafer. To enhance the output signal-to-noise ratio and enable independent operation, a typical rectangular unit cell was designed, featuring a 5×5 arrays of piezoelectric sensing elements connected in parallel[38]. The micromachining process was streamlined to employ only three chromium masks (M1-M3), as detailed in Supplementary Fig. S18. Figure 4a presents an optical photograph of the completed wafer-level transducer surface. Each sensing element pattern consists of a stacked piezoelectric functional layer and a top electrode (*t* = ~1.2 μm, *r* = 200 μm), as shown in the magnified views in Fig. 4b-d. To release the sensing diaphragm, the backside silicon was effectively etched to create a cavity with a diameter of 500 μm and a depth of 620 μm (Fig. 4e-h). The measured cavity-to-piezoelectric film radius ratio is approximately 1.25, in excellent agreement with the finite element simulation results and demonstrating the high precision of our MEMS fabrication process. A micrograph of the single chip containing 25 sensing elements is presented in Supplementary Fig. S19, showcasing a compact footprint with an area of only ~36 mm^2 (Supplementary Fig. S20). This "three-mask and four-etching" manufacturing protocol minimizes error accumulation and ensures high fabrication reliability and batch consistency.

The electrical integrity of the bare chips was initially evaluated using a probe station by connecting the electrodes to two probes (Fig. 4i). The continuity between top electrodes (top-top) and bottom electrodes (bottom-bottom) is illustrated in Fig. 4j. We observed ideal Ohmic contact behavior with excellent conductivity, characterized by low resistance values of 8.05 Ω for the top electrodes and 5.67 Ω for the bottom electrodes. This high electrode continuity across the wafer provides a reliable foundation for low-loss piezoelectric signal transmission. To evaluate the leakage and resistive performance of the RTA-

AlScN film itself, current-voltage (*I-V*) measurements were conducted between the top and bottom electrodes. Under a bias voltage of 5 V, the inter-electrode insulation consistently exceeded 4×10^9 Ω across ten consecutive measurements (Fig. 4k), confirming the high-quality insulation and structural integrity of the annealed film. Figure 4l shows the impedance and phase spectra of the RTA-AlScN unit. The measured resonant frequency of 368.2 kHz is only 5.2% higher than the simulated value (349.0 kHz), validating the accuracy of our design parameters and the effectiveness of the device in responding to low-frequency signals. The overall yield of functional bare dies exceeds 90%, with isolated failures (such as edge-effect-included shorts) occurring only at the wafer periphery.

To optimize the overall sensing performance, a specialized matching circuit and protective packaging were developed. A preamplifier circuit with a gain of 40 dB was fabricated to amplify the weak acoustic-induced charges (Supplementary Fig. S21-S23). For system-level measurements, the MEMS chips were wire-bonded to a printed circuit board (PCB) using a Gold Wire ball bonder, ensuring stable electrical and mechanical interconnections (Supplementary Fig. S24, S25). Finally, the sensors encapsulated using silicone oil and polyurethane to achieve high sensitivity and environmental robustness, as displayed in Supplementary Fig. S26.

2.4 Acoustic receiving performance of MEMS sensor

The packaged MEMS sensor was fully characterized using industry-standard calibration instrument. The operational principle of the sensor is illustrated in Fig. 5a. During underwater deployment, acoustic waves from the environment penetrate the protective shell and the liquid insulating medium to reach the sensitive MEMS diaphragm. The integrated AlScN chips convert the incident acoustic pressure into electrical signals, which are subsequently amplified and processed.

The receiving sensitivity, a critical performance metric, was evaluated using the configuration shown in Supplementary Fig. S27. As demonstrated in Fig. 5b, the sensor exhibits a remarkably flat sensitivity response across the 10 Hz to 1000 Hz operational bandwidth, with a sensitivity of -172.2 dB at 1 kHz. Notably, the sensitivity reaches as high as -162.4 dB at 10 Hz, significantly outperforming conventional AlN-based devices (-178 dB re: V μPa^{-1})[39], thereby highlighting the enhanced acoustic reception enable by the RTA-AlScN film. Time-domain measurements (Supplementary Fig. S28) reveals a stable and clean sinusoidal output voltage, confirming distortion-free signal acquisition and amplification. Furthermore, the self-noise equivalent pressure spectral level, which dictates the detection threshold for weak signals, was analyzed (Fig. 5c). The self-noise amplitude decreases rapidly from 20 Hz to 1 kHz before leveling off above 2.7 kHz. At 1kHz, the noise floor is approximately 59 dB (re:1 μPa $Hz^{-0.5}$), which is comparable to the ambient ocean noise level under Sea State 2[40]. To assess the spatial response, the directivity was measured in both vertical and horizontal planes (Fig. 5d, e). The measured fluctuation was only -1.51 dB and -1.07 dB for the vertical and horizontal planes, respectively, confirming the excellent omnidirectional characteristics of the device.

The receiver's capability was further evaluated through pitch-catch measurements using a PZT ceramic transmitter. In liquid media (water and silicone oil), the peak-to-peak voltage output (V_{PP}) follows a predictable attenuation pattern as the distance from the sound source increases (Fig. 5f, g), consistent with acoustic propagation loss and the decay of particle vibration amplitude[41]. To verify the potential for high-temperature applications, measurements were performed at various temperatures up to 150 °C. Although the V_{PP} values exhibit a marginal decreasing trend with a 12% loss (from 890 mV_{PP} to 800 mV_{PP} at 150 °C), the performance remains highly stable within this range. This robustness indicates that the sensor is well-suited for harsh environments, such as deep-sea offshore wells, automotive underhood sensing, and oil shale exploration[42,43].

Additionally, the sensor's versatility was demonstrated in solid media by coupling the device to a ceramic panel. As the medium layer thickness increased from 2 mm to 15 mm (Fig. 5h), the V_{pp} signal exhibited a monotonic decrease, mirroring the behavior observed in liquid medium. The maximum output voltage of 900 mV observed in silicone oil is attributed to optimal impedance matching between the sensor's internal insulating liquid and the external medium (Supplementary Table S4). For practical applications, long-term stability is paramount. As shown in Fig. 5i, the device demonstrates exceptional sensitivity stability in seawater; after six months of continuous immersion, the cumulative attenuation was only 2.8 dB. This validates the effectiveness of the polyurethane/silicone oil packaging in protecting the core MEMS chip.

To contextualize the achievement in MEMS receivers, a comprehensive comparison of key performance metrics between this work and state-of-the-art reported devices is summarized in Table 1. Notably, our RTA-AlScN MEMS receiver represents a significant breakthrough, being the first to achieve the highest reported sensitivity at such an ultra-low frequency. The following salient merits underscore its potential as a paradigm-shifting solution for low-frequency acoustic sensing. (i) Industrial Scalability: While the majority of prior research has focused on small-scale laboratory prototypes, our work leverages an industrial-grade 6-inch wafer platform. This transition from chip-level to wafer-level fabrication demonstrates the immense potential for high-volume mass production. (ii) Manufacturing Efficiency: The device utilizes a streamlined "three-mask and four-etching" protocol. This minimalist process significantly reduces error accumulation and production costs while ensuring exceptional fabrication reliability and yield. (iii) Record-breaking Sensitivity: To the best of our knowledge, the RTA-AlScN MEMS sensor demonstrates a record-breaking sensitivity of -162.4 dB at the lowest operating frequency of 10 Hz reported to date. This capability addresses a critical gap in detecting infrasonic signals with high fidelity. (iv) Proven Long-term Stability: For the first time in lead-free piezoelectric MEMS research, we report a cumulative sensitivity attenuation as low as 2.8 dB over six months of seawater immersion. This exceptional wet-storage stability validates the effectiveness of our system-level packaging and highlights its readiness for sustained service in harsh marine environments.

Table 1 | Comparisons of sensing performances of our RTA-AlScN receiver with other reported representative MEMS devices

Thin films	Wafer size (inch)	Etching count	Masks	Usable frequency range (Hz)	Highest sensitivity (dB re 1 V μPa^{-1})	Noise resolution (dB re 1 $\mu Pa\ Hz^{-0.5}$ at 1000 Hz)	Directivity	Ref.
PZT	_	6	_	100 -10000	-227.5 @ 2000 Hz	_	_	51
PZT	_	5	5	80-20000	-189.3 @ 920 Hz	_	Omnidirectional	12
PZT	_	_	_	10 -5000	-195.5 @ 2500 Hz	_	_	11
AlN	4	3	4	10-10000	-166.5 @ 750 Hz	40	_	52
AlN	_	4	4	10-8000	-178 @ 1000 Hz	58.7	Omnidirectional	38
AlN	_	6	6	10-1600	-178 @ 1000 Hz	52.6 @ 100 Hz	Omnidirectional	39
AlN	_	4	_	20-1000	-177.6 @ 1000 Hz	58.4	_	10
$Al_{0.905}Sc_{0.095}N$	_	_	_	20000 -160000	-175 @160 kHz	_	Omnidirectional	53
$Al_{0.8}Sc_{0.2}N$	_	4	3	10 -200000	-172 @ 1000 Hz	_	Omnidirectional	54
$Al_{0.8}Sc_{0.2}N$	_	_	_	10 -1000	-162.9 @ 1000 Hz	46.1	Omnidirectional	55

RTA-AlScN	6	4	3	10-1000	-162.4 @10 Hz	59	Omnidir-ectional	This work

3. Conclusion

In summary, we have successfully demonstrated an ultra-sensitive piezoelectric MEMS receiver by a multi-scale lattice engineering strategy. By integrating high-performance AlScN thin film via an industrial-grade fabrication process on 6-inch SOI wafers, we provide a compelling pathway for the development of next-generation ultra-sensitive, low-frequency acoustic devices. The $Al_{0.9}Sc_{0.1}N$ thin film, optimized via post-growth RTA, exhibits significantly enhanced piezoelectric properties, including a d_{33} of 15.0 pC N^{-1} and **a** k_t^2 of 34.9%. This record-breaking performance is fundamentally rooted in a synergistic mechanism: at the atomic scale, Sc-doping reduces the bond covalency and minimum electron density; at the mesoscopic scale, RTA minimizes the lattice parameter ratio (*c*/*a*) and homogenizes nanoscopic domain orientations. **By leveraging** optimized structural design and a robust “three-mask, four-etch” micromachining process, we have established a reliable scalable wafer-level manufacturing route. The resulting MEMS receiver demonstrates unprecedented acoustic responsiveness, highlighted by a record-high sensitivity of -162.4 dB (re: 1 V μPa^{-1}) at 10 Hz, a noise equivalent pressure of 59 dB (re: 1 μPa $Hz^{-0.5}$) at 1 kHz, and omnidirectional receiving characteristics. Furthermore, the device maintains outstanding long-term stability with minimal attenuation over six months of seawater immersion and reliable functionality up to 150 °C. This work underscores the critical synergy between fundamental materials physics, optimized device architecture, and robust system integration, paving a transformative framework for designing high-performance lead-free piezoelectric microsystems in demanding sensing applications.

4. Experiments and computational modelling

The development of the AlScN-based MEMS receiver proceeded through three integrated stages: (i) deposition of high-quality AlScN films on 6-inch SOI wafers, (ii) micromachining of the MEMS sensing units, and (iii) system-level integration and packaging (Supplementary Fig. S29).

4.1 Procedure of AlScN film

P-type (100)-oriented silicon-on-insulator (SOI) wafers (6-inch diameter, resistivity: 0.002-0.005 Ω cm) were employed as substates. The wafer architecture comprises a 5 μm device silicon layer, a 0.5 μm buried oxide (SiO_2) layer, and a 625 μm handle silicon layer. Initially, the SOI wafers underwent Standard Radio Corporation of America (RCA) Cleaning to ensure a pristine surface. Subsequently, a multilayer stack consisting of a seeding layer (20 nm AlN), an adhesion layer (20 nm Cr), a bottom electrode (250 nm Mo), the functional piezoelectric layer (1 μm AlScN), a second adhesion layer (20 nm Cr), and a top electrode (200 nm Mo) was sequentially deposited using a magnetron sputtering system (Explorer 14, DENTON Vacuum LLC, USA). The AlN and AlScN were synthesized under a base pressure of < 5 × 10^{-4} Pa

and a working pressure of 0.4 Pa, with an RF power of 350 W and a substrate rotation of 15 rpm. To optimize piezoelectricity, the as-deposited AlScN films were subjected to rapid thermal annealing at 700 °C.

4.2 Fabrication of the MEMS by micromachining technology

The MEMS fabrication followed a “three-mask and four-etching” protocol on a commercial production line. First, the top electrode and piezoelectric layers were patterned using Mask M1. The Cr/Mo top electrode was defined via Ion Beam Etching (IBE), followed immediately by inductively coupled plasma (ICP) etching of the AlScN layer. The photoresist (AZ 5214, Merck KGaA, Germany) was stripped using AZ400T. Second, a 200 nm SiO_2 insulating layer was deposited via plasma-enhanced chemical vapor deposition (PECVD), and contact holes were patterned using Mask M2 via reactive ion etching (RIE). Third, the interconnection metal was patterned. Finally, the handle Si was etched from the backside using deep reactive ion etching (DRIE, SPTS Rapier, UK) to release the diaphragms. The wafer was diced (NANO 150G), and the resulting chips were mounted onto printed circuit boards (PCB) using epoxy and electrically interconnected via gold wire bonding (53XX BDA, F&S Bondtec, Germany).

4.3 Preparation of AlScN MEMS sensor

To minimize system-level noise, the MEMS chip was integrated with a custom-designed 40 dB preamplifier circuit. Based on acoustic transmission theory, the device was encapsulated using polyurethane and silicone oil. Silicone oil was injected into the sensing cavity to ensure acoustic coupling and hydrostatic pressure balance. The acoustic impedance gradient among seawater (1.57 MRayl), polyurethane (1.62 MRayl), and silicone oil (1.26 MRayl) were optimized to maximize the acoustic-electric conversion efficiency (Supplementary Table S4 and Fig. S30).

4.4 Characterization

Morphological and element distributions were analyzed using SEM (GeminiSEM 360, Carl Zeiss, Germany) and EDS. Crystalline phases were identified via XRD (D8 Advance, Bruker, Germany) using Cu Kα radiation. The quasi-static d_{33} was measured using a d_{33} meter (ZJ-6A, Institute of Acoustics, Chinese Academy of Sciences, China). Impedance spectra, including resonant and anti-resonant frequencies were acquired using an Agilent 4294A analyzer. Electrode conductivity was verified via four-point probe measurements (Crexbox, Deyi Tech). For pitch-catch characterization, a function generator (AFG31000, Tektronix, USA) and oscilloscope (MDO34, Tektronix, USA) were used to record the acoustic response at 20 Hz. Ferroelectric properties and *C-V*/*P-E* loops were characterized using a Radiant Precision Multiferroic system. To facilitate through-thickness poling of the 1-μm-thick films, samples were thinned to ~100 nm using focused ion beam (FIB, Helios G4, USA) milling. The surface morphology was characterized using an atomic force microscope (AFM; Dimension Icon, Bruker, Germany). Following this, the amplitude and phase images of both AG-AlScN and RTA-AlScN films were acquired using the AFM system (Dimension Icon, Bruker, Germany) in piezoelectric mode. Atomic-scale imaging was performed

via HAADF-STEM (Spectra 300, Thermo Fisher Scientific, USA) at 300 kV with an 11 mrad convergence angle.

4.5 Finite element models

Multiphysics simulations were conducted with finite element models, coupling the *Pressure Acoustics*, *Solid Mechanics*, and *Electrostatics* modules. The sensing area was defined by the top electrode geometry. A background pressure field of 1 Pa was applied to evaluate the acoustic-to-electric conversion efficiency via surface charge density analysis.

4.6 DFT calculations

The atomic properties and electronic structure of the materials were calculated using first-principles simulations within density functional theory (DFT)[44]. The projected augmented wave pseudopotentials method was used as implemented in the Vienna *Ab* initio Simulation Package[45]. The exchange correlation energy was calculated using the generalized gradient approximation of the Perdew-Burke-Ernzerhof form[46]. The plane wave cutoff energy was set to 500 eV. For Brillouin zone sampling, a Monkhorst-Pack *k*-point mesh with a spacing finer than 0.03 $Å^{-1}$ was used for all structures[47]. Utilizing the conjugate gradient method, the plane lattice constant and atomic coordinates were fully relaxed until the energy and force converge to 10^{-7} eV and 10^{-3} eV $Å^{-1}$, respectively. The valence electron configurations were set to Sc-$2s^2p^63d^14s^2$, Al-$3s^23p^1$, and N-$2s^22p^3$. The piezoelectric e_{ij} tensors were predicted by the density-functional perturbation theory method[48-50].

Declarations

Data availability

The data that support the findings of this study are available from the corresponding author upon reasonable request.

Acknowledgements

This work was supported by the National Natural Science Foundation of China (Grant Nos. 51972144, U24A2040), the Key Technology Research and Development Program of Shandong Province (Grant No. 2022CXPT045), the Taishan Scholar Foundation of Shandong Province (Grant No. tstp20221130), Taishan Industrial Experts Program (Grant No. tscx202306035), and the 111 Project of International Corporation on Advanced Cement-based Materials (Grant No. D17001).

Author contributions

Z.Y. Cheng, T. Liu, and D. Su contributed equally to this work, leading the majority of the experiments and data analysis. C. Wu contributed to theory and discussions. Y. Liu provided project funding support. W. Sun performed the density functional theory (DFT) calculations. S. Huang supervised this study. C. Yang

and Z. X. Cheng oversaw the conceptualization and design of the study, and led the writing and revision of the manuscript.

Competing interests

The authors declare no competing interests.

Additional information

Supplementary information The online version contains supplementary material available.

References

1. Wang, Q. et al. MEMS acoustic sensors: charting the path from research to real-world applications. *Micromachines* **16**, 43 (2024).
2. Algamili, A. S. et al. A review of actuation and sensing mechanisms in MEMS-based sensor devices. *Nanoscale res. lett.* **16**, 16 (2021).
3. Liu, T. et al. Self-poled bismuth ferrite thin film micromachined for piezoelectric ultrasound transducers. *Adv. Mater.* **37**, 2414711 (2024).
4. Yang, H. et al. AlScN film based piezoelectric micromechanical ultrasonic transducer for an extended long-range detection. *Micromachines* **13**, 1942 (2022).
5. You, Z. et al. Piezoelectric MEMS microphones based on rib structures and single crystal PZT thin film. *Microsyst. Nanoeng*. **10**, 167 (2024).
6. Ba Hashwan, S. S. et al. A review of piezoelectric MEMS sensors and actuators for gas detection application. *Discover Nano* **18**, 25 (2023).
7. Tang, H.-Y. et al. 3-D ultrasonic fingerprint sensor-on-a-chip. *IEEE J. Solid-State Circuits* **51**, 2522–2533 (2016).
8. Muscalu, G. et al. Piezoelectric MEMS energy harvester for low-power applications. *Electronics* **13**, 2087 (2024).
9. Moisello, E. et al. PMUT and CMUT devices for biomedical applications: A Review. *IEEE Access* **12**, 18640–18657 (2024).
10. Zhang, Y., Yang, H., Chen, Z., Sun, F. & Mao, B. Design and analysis of MEMS piezoelectric hydrophone based on signal-to-noise ratio. *IEEE Sens. J.* **25**, 11314–11322 (2025).
11. Liu, D., Zhang, L., Zhang, M. & Zhang, H. A MEMS piezoelectric hydrophone with high sensitivity and wide bandwidth. *Phys. Scr.* **99**, 095918 (2024).
12. Shi, S. et al. Design and fabrication of a novel MEMS piezoelectric hydrophone. *Sens. Actuator A Phys.* **313**, 112203 (2020).
13. Ali, W. R. & Prasad, M. Design and fabrication of piezoelectric MEMS sensor for acoustic measurements. *Silicon* **14**, 6737–6747 (2021).

14. Abels, C. et al. Nitride-based materials for flexible MEMS tactile and flow sensors in robotics. *Sensors* **17**, 1080 (2017).
15. Schwartz, R. W., Dimos, D., Lockwood, S. J. & Torres, V. M. Electrical properties of sol-gel PZT thin films for decoupling capacitor applications. *MRS Online Proceedings Library (OPL)* **310**, 59–64 (1993).
16. Zhang, L. et al. Design and fabrication of high-performance piezoelectric micromachined ultrasonic transducers based on aluminum nitride thin films. *Micromachines* **15**, 1001 (2024).
17. Li, C. et al. Low-Temperature layer-by-layer epitaxy of ferroelectric $Al_{0.63}Sc_{0.37}N$ thin films for back-end-of-line integration. *Nano Lett.* **25**, 16356–16365 (2025).
18. Fichtner, S., Yassine, M., Van de Walle, C. G. & Ambacher, O. Clarification of the spontaneous polarization direction in crystals with wurtzite structure. *Appl. Phys. Lett.* **125**, (2024).
19. Zhang, Y., Zhu, Q., Tian, B. & Duan, C. New-generation ferroelectric AlScN materials. *Nano-Micro Lett.* **16**, 227 (2024).
20. Zhang, Q. et al. Deposition, characterization, and modeling of scandium-doped aluminum nitride thin film for piezoelectric devices. *Materials* **14**, 6437 (2021).
21. Fu, Y. Q. et al. Advances in piezoelectric thin films for acoustic biosensors, acoustofluidics and lab-on-chip applications. *Prog. Mater. Sci.* **89**, 31–91 (2017).
22. Nguyen, T. et al. Large built-in fields and tunable ferroelectricity in composition-graded ScAlN thin films deposited by reactive sputtering. *Adv. Sci.* **12**, 2500611 (2025).
23. Rudresh, J., Sandeep, S., Venugopalrao, S. N. & Nagaraja, K. K. Impact of Sc-doping on structural, phase purity, and dielectric properties of AlN thin films. *J. Appl. Phys.* **137**, 095306 (2025).
24. Ledesma, E., Zamora, I., Uranga, A. & Barniol, N. 9.5 % scandium doped ALN PMUT compatible with pre-processed CMOS substrates. In: *2021 IEEE 34th International Conference on Micro Electro Mechanical Systems (MEMS)*) , 887-890 (2021).
25. Akiyama, M. et al. Enhancement of piezoelectric response in scandium aluminum nitride alloy thin films prepared by dual reactive cosputtering. *Adv. Mater.* **21**, 593–596 (2009).
26. Wu, D. et al. Atomic origins of leakage paths in epitaxial $Al_{1-x}Sc_xN$ thin films. *Nano Lett.* **25**, 14371–14376 (2025).
27. Liu, C. et al. Evaluation of the impact of abnormal grains on the performance of $Sc_{0.15}Al_{0.85}N$-based BAW resonators and filters. *J. Micromech. Microeng.* **32**, 034002 (2022).
28. Wei, Z. et al. The evolution of preferred orientation and morphology of AlN films under various sputtering parameters. *J. Cryst. Growth* **625**, 127439 (2024).
29. Cohen, A. et al. Local environment of Sc and Y dopant ions in aluminum nitride thin films. *ACS Appl. Electron. Mater.* **6**, 853–861 (2024).
30. Shao, S. et al. High quality co-sputtering AlScN thin films for piezoelectric lamb-wave resonators. *J. Microelectromech. Syst.* **31**, 328–337 (2022).

31. Wong, S. J. Z., Roy, K., Lee, C. & Zhu, Y. Thin-film piezoelectric micromachined ultrasound transducers in biomedical applications: A Review. *IEEE Trans. Ultrason., Ferroelectr., Freq. Control* **71**, 622–637 (2024).
32. Daoust, P., Côté, M., Desjardins, P. & Masut, R. A. Impact of applied biaxial stress on the piezoelectric, elastic, and dielectric properties of scandium aluminum nitride alloys determined by density functional perturbation theory. *AIP Adv*. **11**, 095017 (2021).
33. Momida, H. & Oguchi, T. Effects of lattice parameters on piezoelectric constants in wurtzite materials: A theoretical study using first-principles and statistical-learning methods. *Appl. Phys. Express* **11**, 041201 (2018).
34. Ambacher, O. et al. Wurtzite ScAlN, InAlN, and GaAlN crystals, a comparison of structural, elastic, dielectric, and piezoelectric properties. *J. Appl. Phys.* **130**, 045102 (2021).
35. Nguyen, M. D., Houwman, E. P., Dekkers, M. & Rijnders, G. Strongly enhanced piezoelectric response in lead zirconate titanate films with vertically aligned columnar grains. *ACS Appl*. *Mater. Interfaces* **9**, 9849-9861 (2017).
36. Tang, H. & Sodano, H. A. Ultra high energy density nanocomposite capacitors with fast discharge using $Ba_{0.2}Sr_{0.8}TiO_3$ nanowires. *Nano Lett.* **13**, 1373–1379 (2013).
37. Jiang, J. et al. Flexible ferroelectric element based on van der Waals heteroepitaxy. *Sci. Adv.* **3**, e1700121 (2017).
38. Jia, L. et al. Design and characterization of an aluminum nitride-based MEMS hydrophone with biologically honeycomb architecture. *IEEE Trans. Electron Devices* **68**, 4656–4663 (2021).
39. Yang, D. et al. A piezoelectric AlN MEMS hydrophone with high sensitivity and low noise density. *Sens. Actuator A Phys.* **318**, 112493 (2021).
40. Wenz, G. M. Acoustic ambient noise in the ocean: spectra and sources. *J. Acoust. Soc. Am.* **34**, 1936–1956 (1962).
41. Fa, L. et al. Investigation of the physical mechanism of acoustic attenuation in viscous isotropic solids. *Micromachines* **13**, 1526 (2022).
42. Lall, P., Kasturi, M., Wu, H., Suhling, J. C. & Davis, E. Microstructural evolution of viscoelastic properties of underfills under sustained high temperature operation. *J. Electron. Packag.* **144**, 021113 (2021).
43. Lv, Y., Chu, W. & Wang, Q. Thermal management systems for electronics using in deep downhole environment: A review. *Int. Commun. Heat Mass Transf.* **139**, 106450 (2022).
44. Kohn, W. & Sham, L. J. Self-consistent equations including exchange and correlation effects. *Phys. Rev.* **140**, A1133–A1138 (1965).
45. Kresse, G. & Furthmüller, J. Efficient iterative schemes forab initiototal-energy calculations using a plane-wave basis set. *Phys. Rev. B* **54**, 11169–11186 (1996).
46. Perdew, J. P., Burke, K. & Ernzerhof, M. Generalized gradient approximation made simple. *Phys. Rev. Lett.* **77**, 3865–3868 (1996).

47. Monkhorst, H. J. & Pack, J. D. Special points for brillouin-zone integrations. *Phys. Rev. B* **13**, 5188–5192 (1976).
48. Resta, R. Macroscopic polarization in crystalline dielectrics: the geometric phase approach. *Rev. Mod. Phys.* **66**, 899–915 (1994).
49. Talley, K. R. et al. Implications of heterostructural alloying for enhanced piezoelectric performance of (Al,Sc)N. *Phys. Rev. Mater.* **2**, 063802 (2018).
50. Hirata, K. et al. Enhancing the piezoelectric performance of nitride thin films through interfacial engineering. *Mater. Today* **83**, 85–95 (2025).
51. Choi, S., Lee, H. & Moon, W. A micro-machined piezoelectric hydrophone with hydrostatically balanced air backing. *Sens. Actuators A Phys.* **158**, 60–71 (2010).
52. Yang, T. et al. Design and implementation of 6 × 6 array piezoelectric AlN hydrophone with high sensitivity. *IEEE Sens. J.* **21**, 26615–26623 (2021).
53. Zhou, Z. et al. A ScAlN piezoelectric high-frequency acoustic pressure-gradient MEMS vector hydrophone with large bandwidth. *IEEE Electron Device Lett.* **43**, 1109–1112 (2022).
54. Jia, L. et al. Design and characterization of a $Sc_{20\%}Al_{1\text{-}20\%}N$-based PMUTs array for an underwater communication system. *IEEE Sens. J.* **24**, 19763–19769 (2024).
55. Meng, F. et al. A Novel AlN/$Sc_{0.2}Al_{0.8}N$-based piezoelectric composite thin-film-enabled bioinspired honeycomb MEMS hydrophone. *Micromachines* **16**, 454 (2025).
56. Nieto Sierra, L. et al. Systematic approach for high piezoelectric AlN deposition. *J. Alloys Compd.* **1008**, 176723 (2024).
57. Anggraini, S. A., Uehara, M., Hirata, K., Yamada, H. & Akiyama, M. Enhancement in piezoelectric responses of AlN thin films by co-addition of Mg and Ta. *Mater. Chem. Phys.* **276**, 125394 (2022).
58. Lu, Y. et al. Elastic modulus and coefficient of thermal expansion of piezoelectric $Al_{1-x}Sc_xN$ (up to x = 0.41) thin films. *APL Mater.* **6**, 076105 (2018).
59. Jiang, W. et al. In situ synchrotron XRD characterization of piezoelectric $Al_{1-x}Sc_xN$ thin films for MEMS applications. *Materials* **16**, 1781 (2023).
60. Matloub, R. et al. Piezoelectric $Al_{1-x}Sc_xN$ thin films: A semiconductor compatible solution for mechanical energy harvesting and sensors. *Appl. Phys. Lett.* **102**, 152903 (2013).
61. Moreira, M., Bjurström, J., Katardjev, I. & Yantchev, V. Aluminum scandium nitride thin-film bulk acoustic resonators for wide band applications. *Vacuum* **86**, 23–26 (2011).
62. Akiyama, M., Kano, K. & Teshigahara, A. Influence of growth temperature and scandium concentration on piezoelectric response of scandium aluminum nitride alloy thin films. *Appl. Phys. Lett.* **95**, 162107 (2009).
63. Mayrhofer, P. M., Euchner, H., Bittner, A. & Schmid, U. Circular test structure for the determination of piezoelectric constants of $Sc_xAl_{1-x}N$ thin films applying laser doppler vibrometry and FEM simulations. *Sens. Actuators A Phys.* **222**, 301–308 (2015).

64. Mertin, S. et al. Non-destructive piezoelectric characterisation of Sc doped aluminium nitride thin films at wafer level. In: *2019 IEEE International Ultrasonics Symposium (IUS)*). IEEE, 2592–2595 (2019).
65. Mihalic, S., Wade, E., Ott, P. & Ambacher, O. Temperature-dependent properties of wurtzite and rock salt $Al_{1-x}Sc_xN$ for applications in BAW resonators. *J. Phys. D: Appl. Phys.* **58**, 053001 (2024).
66. Mo, D., Dabas, S., Rassay, S. & Tabrizian, R. Complementary-switchable dual-mode SHF scandium aluminum nitride BAW resonator. *IEEE Trans. Electron Devices* **69**, 4624–4631 (2022).
67. Sundarapandian, B. et al. Influence of growth temperature on the properties of aluminum nitride thin films prepared by magnetron sputter epitaxy. *J. Appl. Phys.* **134**, 185107 (2023).
68. Soutome, T. & Yanagitani, T. A method to estimate k_t^2 of piezoelectric films from the change of lattice strain by XRD without removing substrate. In: *2019 IEEE International Ultrasonics Symposium (IUS)*). IEEE, 301–304 (2019).

Figures

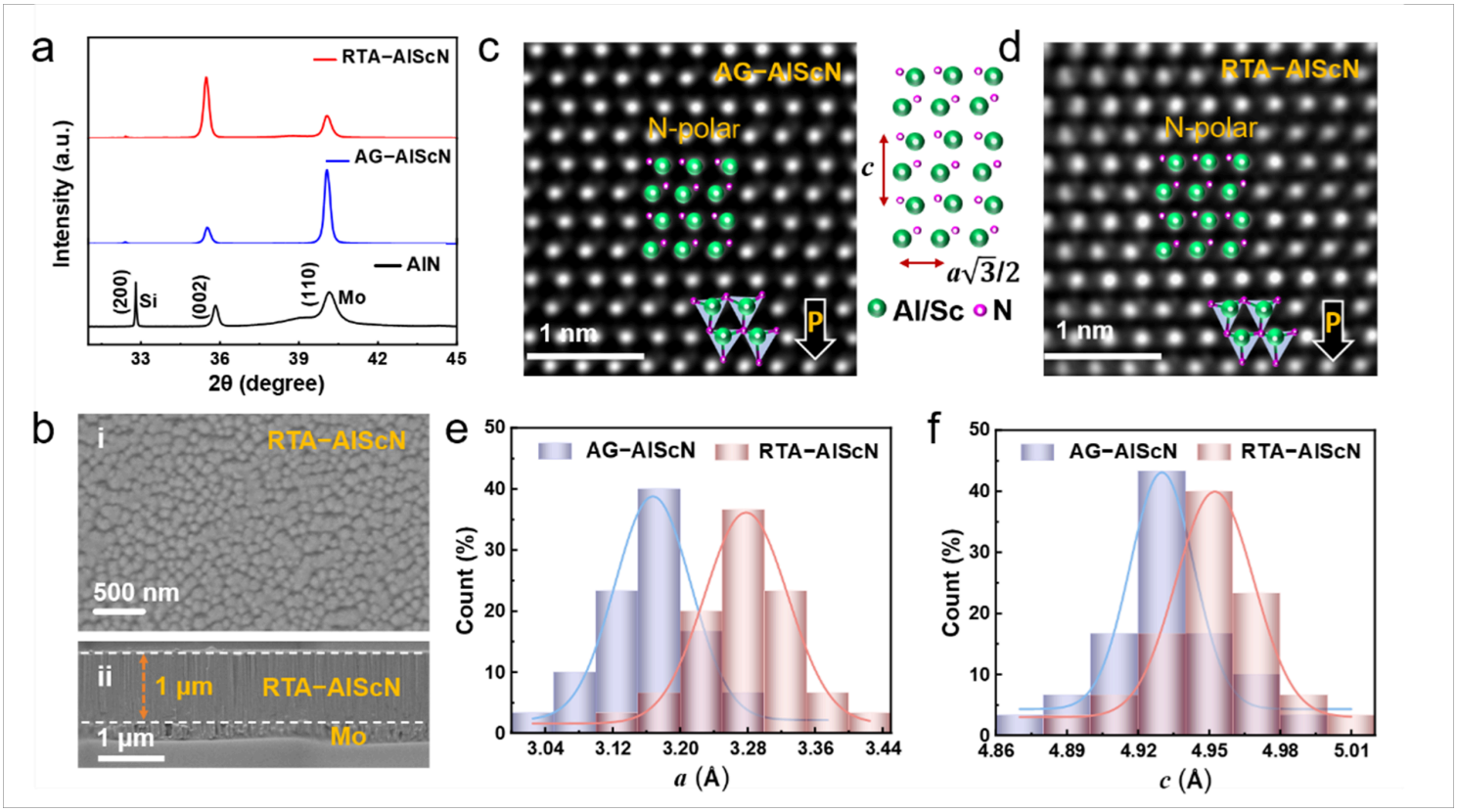


Figure 1

Structural and morphological characterization of AlScN thin films. a) XRD patterns of the AlN, AG-AlScN and RTA-AlScN thin films. b) Surface morphology and cross-sectional SEM images of RTA-AlScN film. c,d) Cross-sectional HAADF-STEM images of revealing the atomic structures of (c) AG-AlScN and (d)

RTA-AlScN. The direction of polarization is indicated by the arrow labeled “P”. e,f) Comparison of lattice parameters of (*a* and *c*) for the AG-AlScN and RTA-AlScN films.

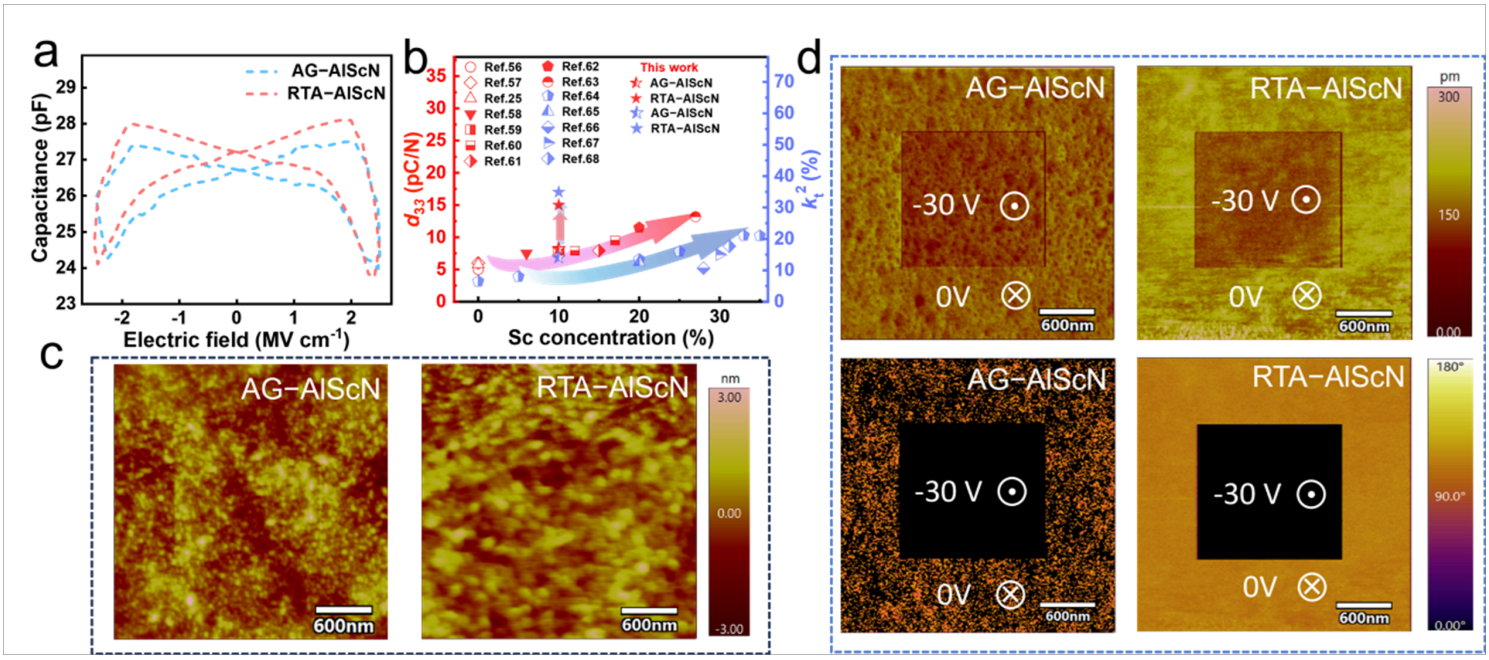


Figure 2

Piezoelectric and ferroelectric characterization of AG-AlScN and RTA-AlScN thin films. a) Capacitance-electric field (*C-E*) loops of the AG-AlScN and RTA-AlScN thin films. b) Comparison of d_{33} and k_t^2 with previously reported AlN-based films[25,56-68]. c) AFM surface morphology of the AG-AlScN and RTA-AlScN thin films. d) Out-of-plane PFM amplitude and phase images of the AG-AlScN and RTA-AlScN thin films. The central 1.5μm × 1.5 μm region was written with a box polarization configuration using a DC tip voltage of -30 V, yielding the polarization reversal from the downward to the upward.

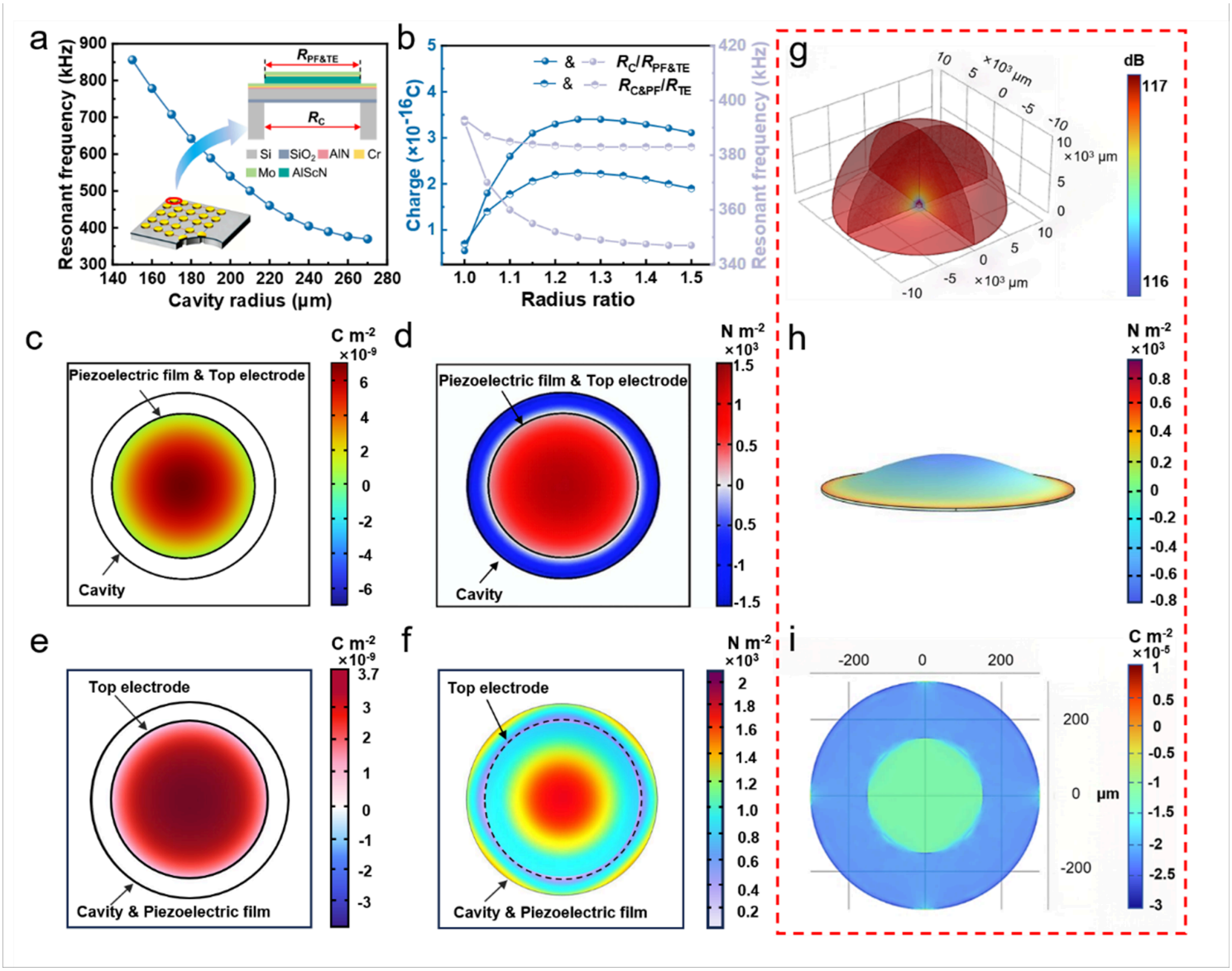


Figure 3

Finite element simulation and structural optimization of the AlScN-based MEMS element. a) Resonant frequency as a function of the back-cavity radius (R_c). The inset shows the chip array and the cross-sectional schematic of a single sensing element. b) Variations of induced charge and resonant frequency across different radius ratios ($R_C/R_{PF\&TE}$ and $R_{C\&PF}/R_{TE}$). c,d) Simulated surface charge density and stress distribution profiles at $R_C/R_{PF\&TE}$=1.25. e,f) Simulated surface charge density and stress distribution profiles at $R_{C\&PF}/R_{TE}$ =1.25. g) Multiphysics model of the acoustic pressure field for excitation. h,i) Resulting stress distribution and surface-induced charge density of the piezoelectric thin film under the acoustic excitation condition defined in g).

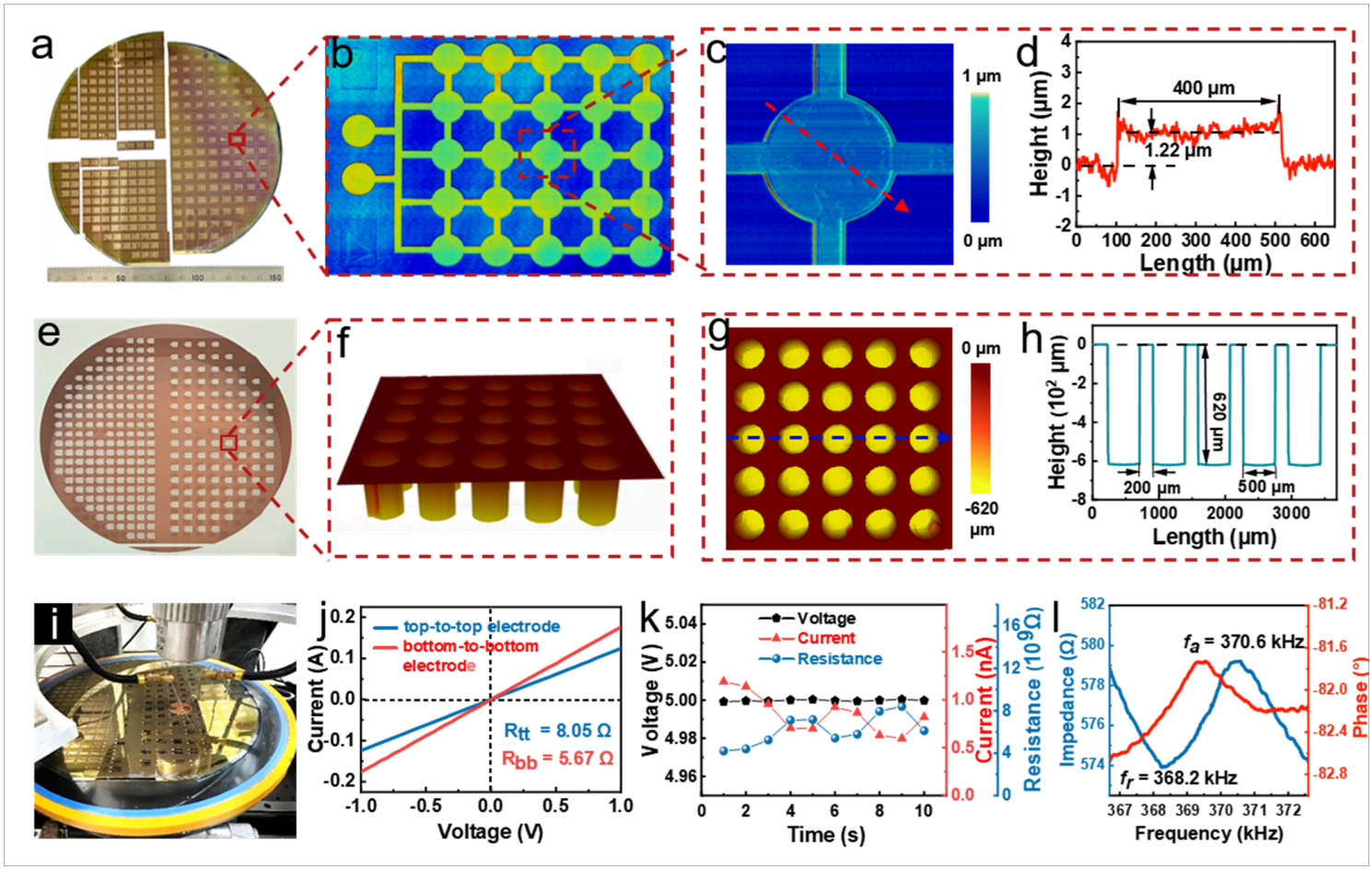


Figure 4

Morphological and electrical characterization of the AlScN-based MEMS chip. a) Optical photograph of the micromachined top surface. b) Magnified view of the 5 × 5 element array. c,d) Three-dimensional topography and corresponding step-height profile of a single sensing element. e) Photograph of the silicon backside after Deep-RIE. f,g) Three-dimensional topography and enlarged view of the etched back-cavity array. h) Cross-sectional profile of the back cavity along the dashed line in g). i) Photograph of the probe-station setup for electrode characterization. j) *I-V* characteristic of the top and bottom electrodes, demonstrating Ohmic contact. k,l) Leakage resistance and impedance spectra of a representative sensing unit, showing a resonant frequency near 368.2 kHz.

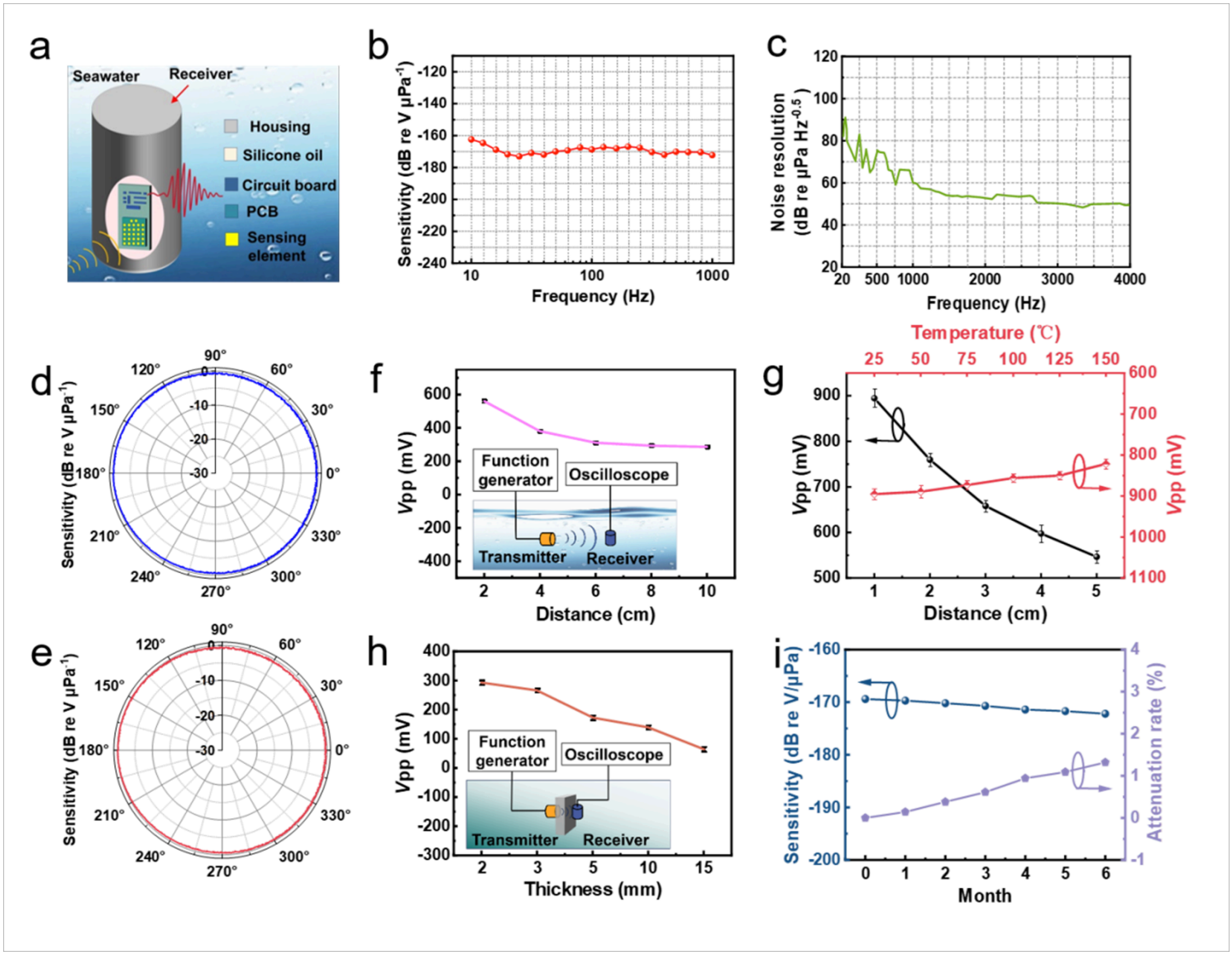


Figure 5

Acoustic receiving performance and environmental robustness of the MEMS receiver. a) Schematic illustration of the operational principle. b) Sensitivity response curve from 10 Hz to 1 kHz. c) Self-noise pressure spectral density level. d,e) Vertical and horizontal directivity patterns. f) Relationship between output voltage amplitude and propagation distance in water. g) Variations of voltage amplitude with distance and temperature in silicone oil. h) Variation of voltage amplitude with ceramic solid medium thickness. i) Long-term sensitivity stability in a shallow-sea environment over six months.

Supplementary Files

This is a list of supplementary files associated with this preprint. Click to download.

- Supplementaryinformation.docx